The interplay of the crystalline electric field and quadrupolar interactions in the spontaneous magnetic phases of $DyIn_3$

2003 J. Phys.: Condens. Matter 15 6269

(http://iopscience.iop.org/0953-8984/15/36/314)

INSTITUTE OF PHYSICS PUBLISHING JOURNAL OF PHYSICS: CONDENSED MATTER

J. Phys.: Condens. Matter **15** (2003) 6269–6283 PII: S0953-8984(03)62910-3

The interplay of the crystalline electric field and quadrupolar interactions in the spontaneous magnetic phases of $DyIn_3$

R M Galéra[1,4], E Sole[1], M Amara[1], P Morin[1,5], P Burlet[2] and A P Murani[3]

[1] Laboratoire Louis-Néel[6], CNRS, BP 166, 38042 Grenoble Cedex 9, France
[2] Magnétisme et Diffraction Neutronique, DRFMC, SPSMS, CEA Grenoble, BP 85X, 38041 Grenoble Cedex 9, France
[3] Institut Laue-Langevin, BP 156, 38042 Grenoble Cedex 9, France

Received 28 April 2003, in final form 31 July 2003
Published 29 August 2003
Online at stacks.iop.org/JPhysCM/15/6269

Abstract

$DyIn_3$ orders at $T_N = 20$ K and undergoes a second spontaneous magnetic transition at 16.5 K. From bulk magnetization measurements, performed on a single crystal along the three main axes of the cubic $AuCu_3$-type structure, the magnetic phase diagrams have been established. The crystalline electric field (CEF) scheme, in the paramagnetic phase, and the magnetic structures of the spontaneous and low field-induced phases have been probed by neutron techniques. All the magnetic phases studied are found to be multiple q with q belonging to the $\langle 1/2, 1/2, 0\rangle$ star. In the low temperature phase ($T < 16.5$ K) the structure is double q with moments along twofold axes, whereas above 16.5 K it becomes triple q with moments along threefold axes. The analysis of the experimental results within the periodic molecular field model leads to a coherent interpretation of the spontaneous magnetic transitions, mainly driven by bilinear exchange and CEF interactions. Though the existence of quadrupolar interactions is definitively proved by the stabilization of multiple q magnetic structures, quadrupolar coefficients are found to be one order of magnitude smaller than those previously reported for $NdIn_3$ and $TbIn_3$.

1. Introduction

Rare earth-based intermetallics are known for their surprisingly wide variety of magnetic properties. In systems where only the 4f ions are magnetic, the interplay between the crystalline electric field (CEF) and just bilinear exchange interactions may result in very

[4] Author to whom any correspondence should be addressed.
[5] Deceased.
[6] Laboratory associated with the Université Joseph-Fourier de Grenoble and the INP Grenoble.

complex behaviours. Complex multiple step or spin-flip metamagnetism is observed in many antiferromagnetic compounds of low symmetry such as tetragonal or hexagonal systems [1]. However in systems where multiaxial magnetic structures stabilize, particularly in cubic ones, it is now well established that couplings involving the 4f charge distribution come into play for a complete understanding of magnetic properties [2]. Within a crystal, as a consequence of the CEF interactions, the 4f shell loses its sphericity. In high symmetry systems however, the degeneracy is not totally removed and electric multipoles (at first order the quadrupoles) are not totally ordered by the CEF. These orbital degrees of freedom are collectively active in the minimization of the total free energy of the system and influence the magnetic properties in both the ordered and paramagnetic phases. Quadrupolar interactions are for instance responsible for the stabilization of the multiple q magnetic structures in cubic antiferromagnets [2, 3]. They lead to complex (H, T) magnetic phase diagrams in many compounds of the CsCl type [4–9], where they are well balanced with the bilinear exchange interactions. Excepting $TmGa_3$ [10], little work has been done on systems with $AuCu_3$-type structure, though several compounds of the RIn_3 series presented complex magnetic behaviours reminiscent of the CsCl-type compounds [11–15]. This motivated the study of the RIn_3 series [16–21].

From previous studies it was known that $DyIn_3$ orders at $T_N = 19.3$ K and undergoes, like $TbIn_3$ [14–21], a second spontaneous transition at $T_* = 17$ K [15]. Moreover magnetization measurements at 4.2 K under high magnetic field (up to 20 T) reveal multiple step processes along the three principal crystallographic axes [11]. To get a more complete insight into the ordered magnetic range properties of $DyIn_3$, we have performed further studies, presented in the present paper. The first section is devoted to the bulk magnetic measurements, performed on a single crystal, and to the determination of the magnetic phase diagrams along the three main axes of the cube. The investigation of the magnetic structures, using neutron diffraction under a magnetic field, is presented in section 2. The knowledge of the CEF scheme is necessary to a quantitative analysis. It was probed by neutron spectroscopy and results are reported in section 3. In the last section we perform an analysis of the different experimental results using the periodic molecular field model in order to achieve a quantitative description of the magnetic properties of $DyIn_3$.

2. Magnetization measurements

The magnetization measurements were performed at the Laboratoire Louis-Néel using an extraction method. Two cryomagnets, which supply magnetic fields up to 11 and 16 T respectively, were used in the temperature range 1.5–300 K. The sensitivity of the measurements reaches 10^{-7} A m^2. The sample is a single crystal of cylindrical shape: 6 mm diameter and 3 mm height. The cylinder axis is parallel to a twofold axis. Isofield and isothermal magnetization curves were measured with the magnetic field applied along the three main axes of the cubic structure.

In the antiferromagnetic phase magnetization measurements confirm the multiple step character of the magnetization processes [11]. Figure 1 shows the magnetization processes measured along the three main axes of the cube at 2 K. When the field is applied along the fourfold and threefold axes, a jump in the magnetization of about 1 μ_B is observed around 4.7 T. No other anomaly is observed up to 9 T and at this field the magnetization reaches only 3.7 μ_B (figure 1). These results are in agreement with those reported in [11]. Along the fourfold axis a small change in the curve slope is evidenced around 1.5 T in the derivative (figure 2). This anomaly, that subsists above T_*, is observed along the fourfold axis only and can be ascribed to domain motions. Along the twofold axis, measurements were performed up to 14.5 T. At 2 K along this axis, the magnetization shows four steps at $\mu_0 H_c = 4.3$, 6.4, 9 and 13.8 T.

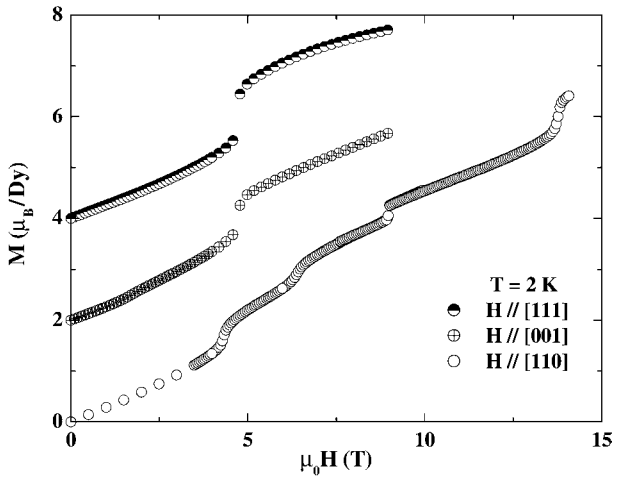

Figure 1. Magnetization curves measured at 2 K for fields applied along the three main symmetry axes of the cubic $AuCu_3$-type structure. For clarity the curves have been offset by 2 μ_B.

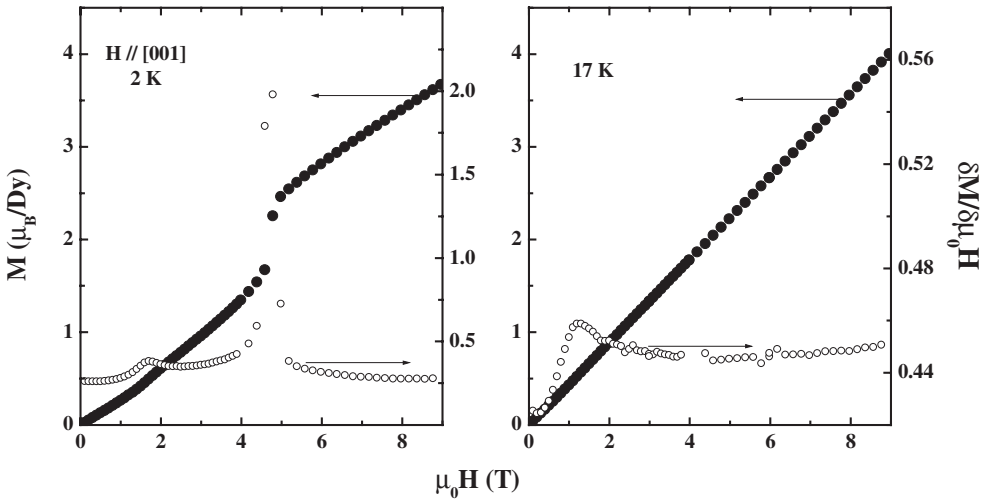

Figure 2. Magnetization curves and derivatives at 2 and 17 K for a magnetic field applied along a fourfold axis.

Under a field of 14.5 T (the limit of the available fields) the magnetization reaches only 6.4 μ_B at 2 K. The value of the fourth critical field, 13.8 T, is smaller than the one reported in [11] ($\mu_0 H_c = 15.5$ T). From the same reference the saturation of the magnetization is reached after this fourth step with a value of 8.67 μ_B. The discrepancy may be explained by the existence of a fifth transition above 14.5 T, which was not resolved in the former measurements. It is worth noting that the present measurements have a better resolution. Along this twofold axis the thermal variations of the magnetization measured under different fields reveal the existence of new transitions, as observed in figure 3 for the curves under 10 or 14.5 T.

From magnetization processes and thermal variations of the magnetization under different fields, the H–T phase diagrams were partly (field limitation) built for the three symmetry axes

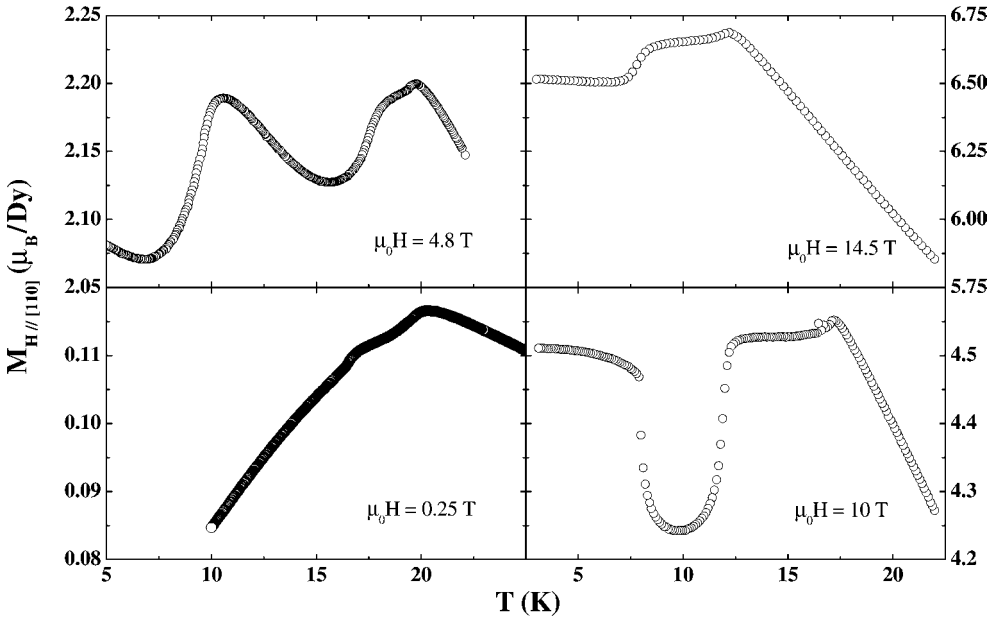

Figure 3. Thermal variation of the magnetization for different values of the field applied along a twofold axis.

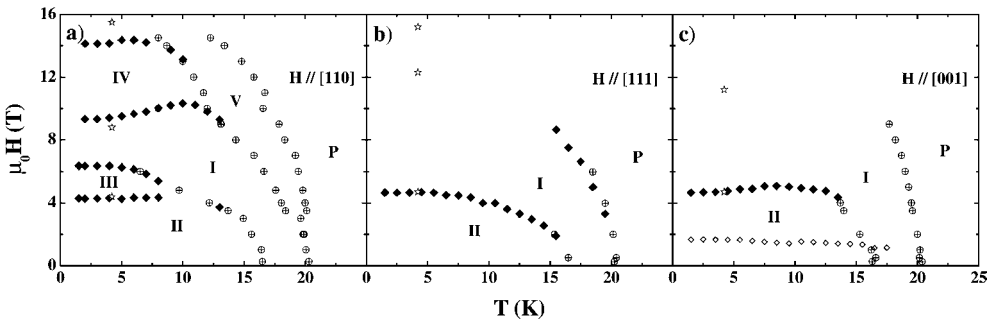

Figure 4. Magnetic phase diagrams of $DyIn_3$ for fields applied along a twofold axis (a), threefold axis (b) and fourfold axis (c). Diamonds represent the features observed on magnetization curves: open diamonds indicate domain effects and full ones critical fields. Open stars represent the values of the critical fields given in [11]. The circles represent the critical temperatures determined from thermal variations.

of the cube (figure 4). Along the twofold axis (figure 4(a)), in addition to the two spontaneous phases, three field-induced magnetic phases are observed. As discussed above and according to [11], a fourth field-induced phase is expected at low temperatures in high fields before reaching the paramagnetic saturated phase. Along the threefold (figure 4(b)) and fourfold axes (figure 4(c)), the measurements were performed only up to 9 T; therefore the evolution of the high field-induced phases could not be followed. The curve represented by open diamonds in figure 4(c) accounts for domain effects as mentioned above. The temperatures of the spontaneous transitions deduced from these diagrams are respectively $T_N = 20.3 \pm 0.3$ K and $T_* = 16.5 \pm 0.3$ K.

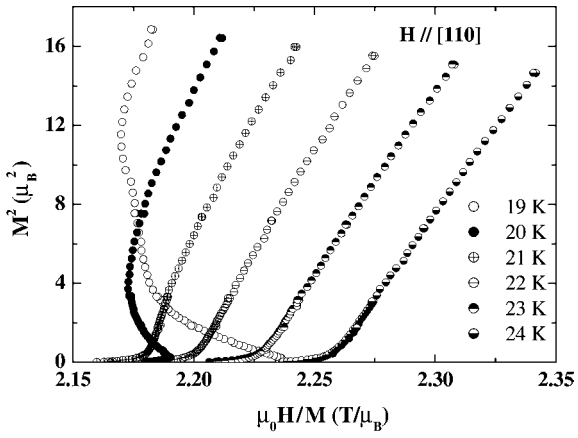

Figure 5. Arrott plots ($M^2 = f(H/M)$) obtained for magnetization curves in fields along a twofold axis.

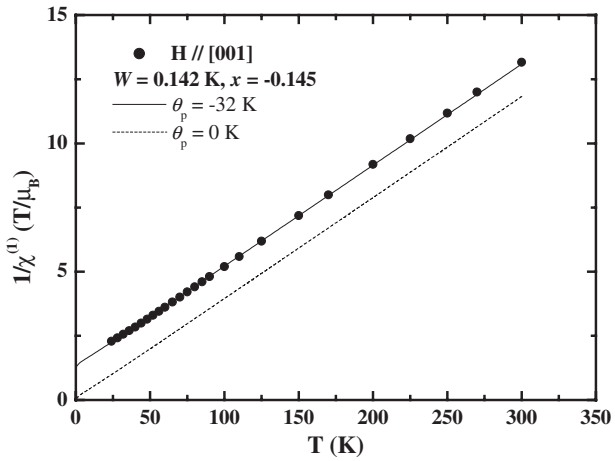

Figure 6. The thermal variation of the inverse of the first order magnetic susceptibility. The dots represent the experimental points determined from the magnetization measurements along the fourfold axis. The lines represent the thermal variation calculated with the set of CEF parameters: $W = 0.142$ K and $x = -0.145$ for $\theta_p = 0$ K (dashed line) and $\theta_p = -32$ K (full line).

In the paramagnetic phase the first and third order magnetic susceptibilities, $\chi^{(1)}$ and $\chi^{(3)}$ respectively, were deduced from Arrott plots, $M^2 = f(H/M)$, that show a linear behaviour in the temperature range 21–300 K (figure 5). In figure 5 are also shown the Arrott plots at 20 and 19 K; they present a change of sign of the initial slope characteristic of the magnetically ordered phase. In the present work, only the plots above 21 K have been used for the determination of the magnetic susceptibilities. At each temperature the intercept of $M^2 = f(H/M)$ with the H/M axis gives the inverse of $\chi^{(1)}$. $\chi^{(3)}$ is deduced from the slope of the Arrott plots using the expression $\chi^{(3)} = -[\chi^{(1)}]^4[\Delta(\mu_0 H/M)/\Delta M^2]$. In figure 6 we present the thermal variation of $1/\chi^{(1)}$. It follows a Curie–Weiss law that intercepts the temperature axis at $\theta_p = -32.6 \pm 1$ K. The effective magnetic moment obtained from the slope of the Curie–Weiss line: $10.59 \pm 0.1\ \mu_B$, is in good agreement with the theoretical value for the Dy^{3+} ion, $\mu_{eff} = 10.646\ \mu_B$. Figure 7 shows the thermal variation up to 100 K of $\chi^{(3)}$, determined

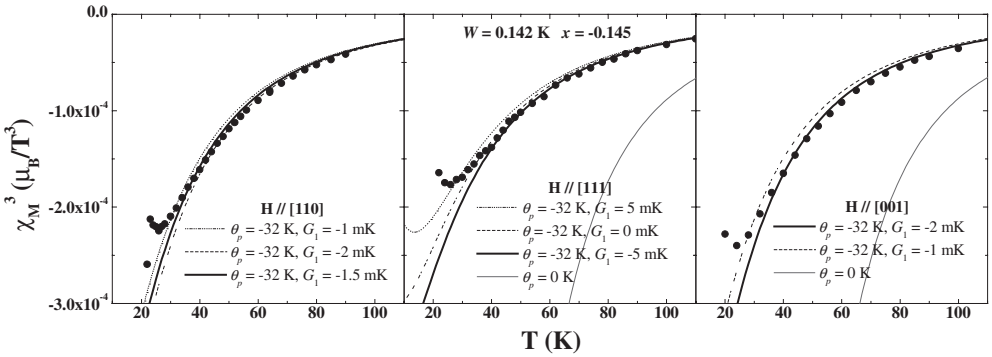

Figure 7. The thermal variation of the third order magnetic susceptibility for fields applied along the three main symmetry axes of the cube. The curves represent the calculations with the set of CEF parameters, $W = 0.142$ K and $x = -0.145$, and the values of the θ_p and G_1 parameters given in the figures.

for fields applied along the [110], [001] and [111] axes. It remains negative over the whole temperature range studied and decreases with the temperature down to 26 K. The upward slope observed below this temperature is probably due to magnetic correlations when getting closer to the ordering temperature. The third order susceptibility presents a slight anisotropy between the threefold and fourfold high symmetry axes. The easy axis appears to be the threefold one.

3. Neutron diffraction

Neutron diffraction experiments were carried out at the CEN-Grenoble reactor SILOE, on the DN3 spectrometer. In order to reduce the absorption, the $DyIn_3$ sample used in this experiment was a long single crystalline needle of 10 mm height and 1 mm diameter, with the twofold axis along the cylinder axis. It was mounted with this axis $[1\bar{1}0]$ vertical and parallel to the magnetic field supplied by a cryomagnet. With this set-up experiments could be performed in the temperature range 1.5–300 K in fields up to 4.8 T. The incident neutron wavelength was 1.521 Å and the moving-up counter allowed us to reach reflections out of the equatorial plane inside the angular range $-5°$–$10°$.

At zero field, three data collections were performed successively at 26, 16.8 (phase I) and 5.8 K (phase II). The thermal evolution of the $(1/2, 1/2, 0)$, $(1/2, 0, 1/2)$ and $(0, -1/2, 1/2)$ magnetic reflections was then followed under several applied fields up to 4.8 T. Before changing the value of the applied field the sample was first warmed up above the Néel temperature, then, for a given field, the measurements of the magnetic integrated intensities were performed while cooling the sample from the paramagnetic phase. Figure 8 shows for instance the thermal variation of the three reflections under 3 and 4.8 T. Irregularities are clearly observed at the transitions between phase I and III under 3 T (figure 8(a)) and phase I and III under 4.8 T, whereas there is no evidence of the phase V–phase I transition at this field (figure 8(b)). Finally two data collections were performed at 2.3 and 13 K under an applied field of 4.8 T.

For each data collection the integrated intensities have been measured for up to 60 non-equivalent reflections. The data were analysed using a least squares procedure. The program calculates and adjusts, for each model of magnetic structure probed, the different domain proportions and the amplitude of the magnetic moment. The reliability factor is given by

$$R = \left(\sum_i^{n_{\text{obs}}} p_i |I^i_{\text{cal}} - I^i_{\text{obs}}| / I^i_{\text{obs}} \right) \Big/ \sum_i^{n_{\text{obs}}} p_i .$$

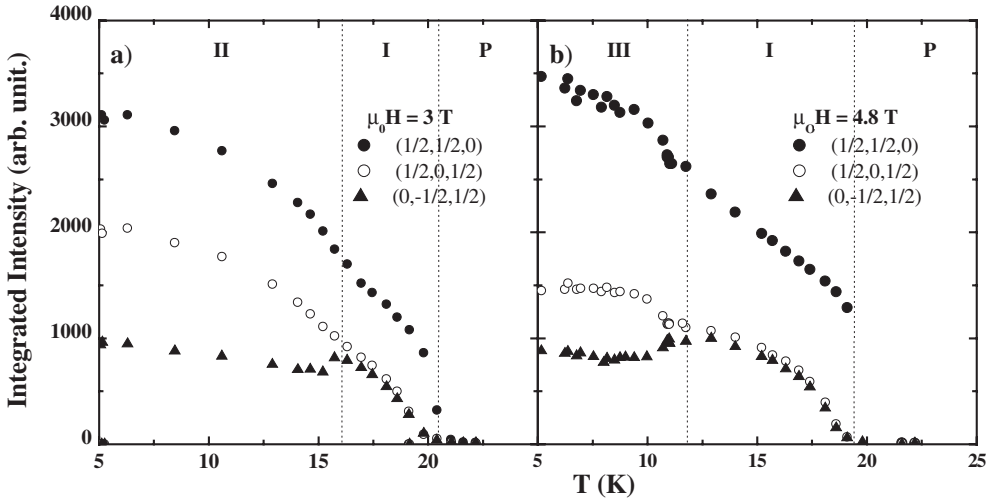

Figure 8. Thermal variation of the integrated intensities of the magnetic reflections, $(1/2, 1/2, 0)$ (full dots), $(1/2, 0, 1/2)$ (open dots) and $(0, -1/2, 1/2)$ (full triangles) under an applied field of (a) 3 T, (b) 4.8 T. In the experiments, the field was applied along the $[1\bar{1}0]$ vertical direction of the single crystal.

Table 1. Refined values of the moment amplitude, $\mathcal{M}$, and domain proportions d_z, d_x and d_y, obtained for the single q structure in the spontaneous phases I and II. The reliability factors of each refinement are given in column 6. For the domain d_z, the Fourier component $\vec{M}_q = (0, 0, 1)$ is associated with the propagation vector $\vec{q} = (1/2, 1/2, 0)$. The magnetic moment at site $\vec{r}_i$, is then given by $\vec{M}(\vec{r}_i) = \mathcal{M}\vec{M}_q \cos(2\pi\vec{q} \cdot \vec{r}_i)$.

T (K)	$\mathcal{M}$ (μ_B)	d_z (%)	d_x (%)	d_y (%)	R (%)
16.8	6.44 ± 0.3	38	31	31	4.8
5.8	8.33 ± 0.4	39	31	30	5.5

n_{obs} is the number of observed reflections and p_i the weight of the reflection i: p_i is the inverse of the statistical error of the observed intensity for reflection i. The models of spontaneous magnetic structures probed in the present calculations are chosen from the inventory of the high symmetry magnetic structures listed by Amara and Morin [3]. In these models it is assumed that (i) the magnetic moment keeps a constant modulus at all sites, (ii) the easy magnetization direction is frozen by the CEF along only one family of high symmetry axes of the cube.

The reliability factor of the refinement of the data collected at 26 K for the $AuCu_3$ structure is $R = 3\%$. This collection of data allowed us also to check the background level at the positions expected for the magnetic satellites and to confirm a contamination of the diffracted intensity by the $\lambda/2$ harmonic less than $1‰$. For the two spontaneous phases (I and II) the refinements give a satisfactory agreement for either (i) a single q structure with the moments along a fourfold axis or (ii) a double q structure with the moments along twofold axes or (iii) a triple q structure with the moments along threefold axes. Tables 1–3 describe respectively these three models via their Fourier components and give the values of the different refined parameters and figure 9 shows the three magnetic structures. Table 4 compares for some reflections the integrated intensity measured at 16.8 K in zero field and the calculated one within the three models. These three models of multiaxial structures lead to the same powder spectra as a collinear structure where the magnetic moments make an angle $\phi = 0°$ with the unique c axis

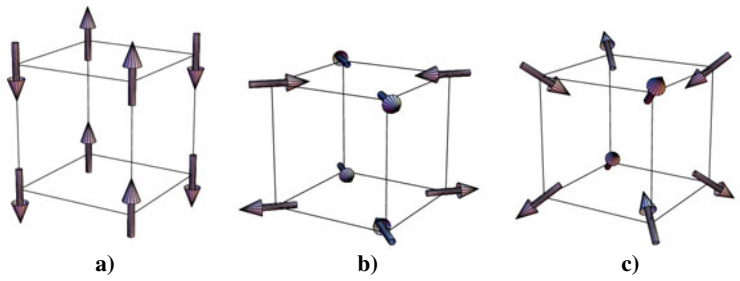

Figure 9. Representations of the three possible spontaneous high symmetry magnetic structures: (a) single q structure with fourfold easy axes, (b) double q structure with twofold easy axes, (c) triple q structure with threefold easy axes.

(This figure is in colour only in the electronic version)

Table 2. Refined values of the moment amplitude, $\mathcal{M}$, and domain proportions d_{xy}, d_{yz} and d_{xz}, obtained for the double q structure in the spontaneous phases I and II. The reliability factors R of each refinement are given in column 6. The structure is determined by the following Fourier components: domain d_{xy}, $\vec{M}_{q_1} = (0, 1/\sqrt{2}, 0)$ with $\vec{q}_1 = (1/2, 0, 1/2)$; $\vec{M}_{q_2} = (1/\sqrt{2}, 0, 0)$ with $\vec{q}_2 = (0, 1/2, 1/2)$; domain d_{yz}, $\vec{M}_{q_1} = (0, 0, 1/\sqrt{2})$ with $\vec{q}_1 = (1/2, 1/2, 0)$; $\vec{M}_{q_2} = (0, 1/\sqrt{2}, 0)$ with $\vec{q}_2 = (1/2, 0, 1/2)$; domain d_{xz}, $\vec{M}_{q_1} = (1/\sqrt{2}, 0, 0)$ with $\vec{q}_1 = (0, 1/2, 1/2)$; $\vec{M}_{q_2} = (0, 0, 1/\sqrt{2})$ with $\vec{q}_2 = (1/2, 1/2, 0)$. At each site the magnetic moment is given by $\vec{M}(\vec{r}_i) = \mathcal{M} \sum_{q_j} \vec{M}_{q_j} \cos(2\pi \vec{q}_j \cdot \vec{r}_i)$.

T (K)	$\mathcal{M}$ (μ_B)	d_{xy} (%)	d_{yz} (%)	d_{xz} (%)	R (%)
16.8	6.40 ± 0.3	26	37	37	4.7
5.8	8.36 ± 0.4	22	38	40	5.5

Table 3. Refined values of the moment amplitude, $\mathcal{M}$, and reliability factor, R, obtained for the triple q structure in the spontaneous phases I and II. This single domain structure is determined by the three Fourier components: $\vec{M}_{q_1} = (0, 0, 1/\sqrt{3})$ with $\vec{q}_1 = (1/2, 1/2, 0)$; $\vec{M}_{q_2} = (0, 1/\sqrt{3}, 0)$ with $\vec{q}_2 = (1/2, 0, 1/2)$; $\vec{M}_{q_3} = (1/\sqrt{3}, 0, 0)$ with $\vec{q}_3 = (0, 1/2, 1/2)$ and the magnetic moment given by $\vec{M}(\vec{r}_i) = \mathcal{M} \sum_{q_j} \vec{M}_{q_j} \cos(2\pi \vec{q}_j \cdot \vec{r}_i)$.

T (K)	$\mathcal{M}$ (μ_B)	R (%)
16.8	6.36 ± 0.3	6.9
5.8	8.09 ± 0.4	9.9

of the $(2a, 2a, a)$ magnetic cell [16]. From previous powder neutron data it was deduced that two multiaxial structures associated with $\phi = 30°$ (triple q with moments along the twofold axes) or $\phi = 35.26°$ (double q with moments along the threefold axes) were alike. Indeed powder pattern refinements led to $\phi = 32°$ [16]. However no reasonable fitting of the present single crystal data could be obtained with either of these two structures. A similar discrepancy between powder and single crystal data analyses has been already observed for $TbIn_3$ [21]. For both compounds it is very probable that powdering the samples induced strong metallurgical stresses and defects.

In order to determine the actual spontaneous structures in phases I and II let us discuss the effects on these structures of a field applied along the $[1\bar{1}0]$ direction assuming that it achieves a complete domain selection and does not distort the structures. In the case of the single q structure (table 1, figure 9(a)), the field favours only the domain d_z associated with the

Table 4. Integrated and calculated intensities for representative reflections measured at 16.8 K in zero field within the three given models of magnetic structures.

	$T = 16.8$ K		Triple q	Double q	Single q
h, k, l	I_{obs}	p_i	I_{cal}	I_{cal}	I_{cal}
1/2, 1/2, 0	1360	50	1169.7	1306.8	1352
1/2, 0, 1/2	1120	50	1169.7	1119.9	1119.3
1/2, 0, −1/2	993	50	1169.7	1119.9	1119.3
0, −1/2, 1/2	1120	50	1169.7	1119.9	1119.6
0, −1/2, −1/2	1050	50	1169.7	1119.9	1119.6
1/2, 1/2, 1	405	25	352.7	393.9	407.4
−1/2, −1/2, 1	394	25	352.7	393.9	407.4
−1/2, −1, 1/2	365	25	352.7	337.7	337.6
−1/2, −1, −1/2	325	25	352.7	337.7	337.6
1, 1/2, 1/2	358	25	352.7	337.7	337.7
1, 1/2, −1/2	367	25	352.7	337.7	337.7
1/2, 0, 3/2	962	33	953.6	913	912.6
0, −1/2, 3/2	978	33	953.6	913	912.8
3/2, 1, 1/2	639	11	623.7	597.2	596.8
3/2, 1, −1/2	666	11	623.7	597.2	596.8
5/2, 2, 1/2	291	5	290.8	278.5	278.4
5/2, 2, −1/2	283	5	290.8	278.5	278.4
5/2, 5/2, 0	433	17	397.5	444	459.3
−5/2, −5/2, 0	337	13	397.5	444	459.3
1, 1, 0	2140	50	2102.9	2102.9	2102.9
−1, −1, 0	2100	50	2102.9	2102.9	2102.9
−1, −2, 0	2100	50	2102.9	2102.9	2102.9
−1, −2, 1	2130	50	2102.9	2102.9	2102.9

$(1/2, 1/2, 0)$ propagation. Consequently the intensities at the $(0, -1/2, 1/2)$ and $(1/2, 0, 1/2)$ positions, associated with the domains d_x and d_y respectively, should vanish. In the case of the double q structure (table 2, figure 9(b)) the field equally favours the d_{xz} and d_{yz} domains. If these two domains present an equal partition within the sample, the $(1/2, 0, 1/2)$ and $(0, -1/2, 1/2)$ satellites should have exactly the same intensity, half that of the $(1/2, 1/2, 0)$ satellite. For non-equal distribution of the domains the sum of the $(1/2, 0, 1/2)$ and $(0, -1/2, 1/2)$ intensities should equal the $(1/2, 1/2, 0)$ intensity. Finally, as the triple q model in table 3 (figure 9(c)) is single domain, the field has no effect and the three satellites should keep an equal intensity in a rigid structure model.

As shown in figure 8(a), the thermal evolution under 3 T of the $(1/2, 1/2, 0)$, $(1/2, 0, 1/2)$ and $(0, -1/2, 1/2)$ intensities is apparently in much better agreement with the evolution expected for the double q rigid structure in phase I ($T_* < T < T_N$): the $(1/2, 1/2, 0)$ intensity remains twice larger than both the $(1/2, 0, 1/2)$ and the $(0, -1/2, 1/2)$ intensities, which are roughly the same. The double q structure is associated with an easy magnetization direction along twofold axes. The stabilization of a twofold axis anisotropy in phase I is however not compatible with a magnetic transition at T_N of second order as is observed in $DyIn_3$ (see figure 3 or [15]). Under 4.8 T, in phase I, the $(1/2, 1/2, 0)$ intensity becomes larger than the sum of the two other reflections (figure 8(b)). It can be also noted that $DyIn_3$ presents an important susceptibility (see figure 2). According to that, it is very likely that either the field is not efficient enough to completely purify the domains or the structure is easily distorted by applying the field.

Table 5. Results of the refinements of the data collected at 13 K under 4.8 T (phase I) within a triple q structure model and taking into account a field-induced distortion ($H \parallel [1\bar{1}0]$). This structure can be described by a ferromagnetic component at the centre of the Brillouin zone: $\vec{M}_0 = F(\sqrt{d_0/2}, -\sqrt{d_0/2}, 0)$ and the three following Fourier components: $\vec{M}_{q_1} = (0, 0, \sqrt{d_1})$ with $\vec{q}_1 = (1/2, 1/2, 0)$; $\vec{M}_{q_2} = (0, \sqrt{d_2}, 0)$ with $\vec{q}_2 = (1/2, 0, 1/2)$; $\vec{M}_{q_3} = (\sqrt{d_3}, 0, 0)$ with $\vec{q}_3 = (0, 1/2, 1/2)$. The magnetic moment at the site $\vec{r}_i$ is given by $\vec{M}(\vec{r}_i) = \mathcal{M}[\vec{M}_0 + \sum_{j=1}^{3} \vec{M}_{q_j} \cos(2\pi \vec{q}_j \cdot \vec{r}_i)]$. The d_i are refined parameters which account for the rate of deformation of the spontaneous triple q structure; they satisfy the relation: $\sum_{i=0}^{3} d_i = 1$. The other refined parameters are: $\mathcal{M}$ the moment amplitude and $\mathcal{F}$ the ferromagnetic reinforcement.

$T = 13$ K, $\mu_0 H = 4.8$ T						
$\mathcal{M}$ (μ_B)	$\mathcal{F}$	d_0	d_1	d_2	d_3	R (%)
7.55 ± 0.4	1.21	0.07	0.22	0.19	0.52	9.4

This is confirmed by the refinements of the data collected at 13 K under a field of 4.8 T (phase I). The best agreement between calculated and observed intensities is obtained for an initially triple q structure model (as presented in table 3) strongly distorted by the field. The Fourier components that describe the structure are given in table 5, together with the refined parameters. According to this structure the component of the magnetization along a twofold axis has been calculated at 13 K under 4.8 T: $M_{\parallel[1,1,0]} = 2.36\ \mu_B$, value in rather good agreement with that of the experimental magnetization, $M(13\text{ K}, 4.8\text{ T}) = 2.16\ \mu_B$.

Such a result strongly supports the stabilization in phase I of the triple q structure with moments along the threefold axes (table 3). The discrepancy between the expected and experimental thermal variation of the magnetic intensities under an applied field, as shown in figure 8, is explained then by the high susceptibility of $DyIn_3$, which leads to a strong ability of the magnetic structures to distort under a field.

Starting from the models of the high symmetry field-induced magnetic structures, the refinements of the data collected in phase III: $T = 2.3$ K, $H = 4.8$ T, converge rapidly, with a reliability factor R of 8%, on a four q structure with normalized moments lying along twofold axes. The description of the structure and the values of all the refined parameters are given in table 6. The calculation of the magnetization along the applied field direction using this model gives $M_{\parallel[1,1,0]} = 2.24\ \mu_B$ at 2.3 K under a field of 4.8 T. Such a value compares well with the one given by the magnetization measurements. As shown in figure 1 the magnetization at 2 K under a field of 4.8 T applied along a twofold direction reaches 2.1 μ_B.

This field-induced phase (phase III) leads to a twofold anisotropy axis. Consequently the stabilization of double q structure in phase II becomes very likely. The spontaneous transition at T_* could then be ascribed to a transition from the triple q structure described in table 3 towards the double q one in table 2.

4. Neutron spectroscopy

Any further analysis requires the knowledge of the CEF scheme in $DyIn_3$. The CEF has been probed in the polycrystalline $(Dy_{0.05}Y_{0.95})In_3$ alloy where no magnetic order is observed down to 1.5 K (temperature limit). Neutron scattering experiments were performed at ILL on the IN6 and IN4 time-of-flight spectrometers. To optimize the scattered intensity the sample was shaped as a plate of 3×5 cm^2 and 1 mm thick. On the high resolution IN6 spectrometer, the spectra were collected at 5, 20, 50 and 100 K with an incident neutron energy of $E_i = 3.12$ meV ($\lambda_i = 5.12$ Å and FWHM = 0.12 meV). Figure 10 shows the inelastic spectrum obtained at 5 K on IN6. In the down-scattering processes only one, but well

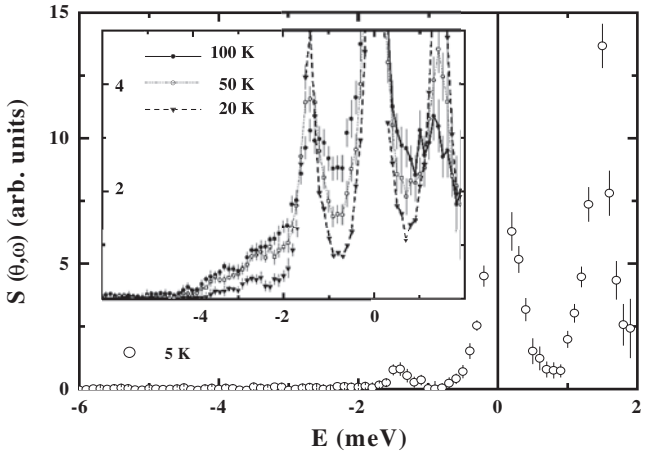

Figure 10. The observed spectrum $S(\theta, \omega)$ for the dilute alloy $(Dy_{0.05}Y_{0.95})In_3$ at 5 K obtained on the IN6 time-of-flight spectrometer. The inset represents the evolution of the spectrum with the temperature.

Table 6. The multiple q structure model for $DyIn_3$ in phase III: $\vec{M}_{q_0} = (1/4\sqrt{2}, -1/4\sqrt{2}, 0)$ with $\vec{q}_0 = (0, 0, 0)$; $\vec{M}_{q_1} = (1/4\sqrt{2}, -1/4\sqrt{2}, 0)$ with $\vec{q}_1 = (0, -1/2, 1/2)$; $\vec{M}_{q_2} = (-1/4\sqrt{2}, 1/4\sqrt{2}, -1/\sqrt{2})$ with $\vec{q}_2 = (1/2, -1/2, 0)$; $\vec{M}_{q_3} = (-1/4\sqrt{2}, -3/4\sqrt{2}, 0)$ with $\vec{q}_3 = (1/2, 0, 1/2)$. This structure gives rise to four different magnetic domains. Its distortion by an applied field along the $[1\bar{1}0]$ direction is accounted for by a ferromagnetic reinforcement factor F. The magnetic moments point along twofold axes and at any site $\vec{r}_i$ they are given by $\vec{M}(\vec{r}_i) = \mathcal{M}[F\vec{M}_0 + \sum_{j=0}^{3} \vec{M}_{q_j} \cos(2\vec{\pi}\boldsymbol{q}_j \cdot \vec{r}_i)]$.

$T = 2.3$ K, $\mu_0 H = 4.8$ T						
$\mathcal{M}$ (μ_B)	$\mathcal{F}$	d_1 (%)	d_2 (%)	d_3 (%)	d_4 (%)	R (%)
8.46 ± 0.4	0.02	16.8	33.2	16.8	33.2	7.9

resolved, inelastic peak is observed at 1.44 meV. The corresponding de-excitation is observed at -1.44 meV in the up-scattering processes. Increasing the temperature (inset in figure 10) the intensity at -1.44 meV progressively increases at the expense of the excitation peak while the scattered signal increases in down- and up-scattering around ± 0.85 meV. In the up-scattering region, a broad and weak feature appears around -2.7 meV at 20 K that progressively increases with temperature. At 50 K another weaker feature appears around -3.6 meV. The search for excitations at higher energies was performed on the IN4 spectrometer with an incident energy of $E_i = 17$ meV ($\lambda_i = 2.2$ Å and FWHM ≈ 1.2 meV) at 5 and 20 K. On the IN4 spectra, the peak at 1.44 meV is confirmed but within the experimental resolution no other excitation is resolved up to 10 meV. All these observations reveal that, apparently, the only transition from the ground state is the one observed at 1.44 meV.

The previous studies on $NdIn_3$ and $TbIn_3$ have clearly demonstrated that the CEF parameters, $A_4\langle r^4\rangle$ and $A_6\langle r^6\rangle$, are positive in both compounds [20, 21]. We are therefore justified in assuming positive CEF parameters in $DyIn_3$ as well. From the diagram of Lea *et al* [22], the W and x parametrized CEF parameters should then satisfy the conditions $W > 0$, $x < 0$. The expected CEF ground state is either the Γ_7 or the Γ_6 doublet and the excitation at 1.44 meV can be ascribed to the $\Gamma_7 \leftrightarrow \Gamma_8^{(1)}$ or the $\Gamma_6 \leftrightarrow \Gamma_8^{(1)}$ transition. Note that the transition

probabilities calculated by Birgeneau [23] in this region of the diagram are quite consistent with the observation of only one transition in the energy range probed. Unfortunately, with only one observed excitation from the ground state, the CEF scheme cannot be determined from just the neutron spectroscopy data.

5. Analysis

The CEF scheme determination was first attempted by checking the magnetic anisotropy in the paramagnetic phase at T_N. The free energy associated with the three main directions of anisotropy in the cube has been calculated using a self-consistent method, for several (W, x) couples in the region $-1 \leqslant x \leqslant 0$. For each value of x, W is adjusted according to the experimental energy of the excitation. At T_N the CEF favours the fourfold easy axis for x ranging between -1 and -0.2 and the twofold axis for $-0.2 \leqslant x \leqslant 0$. In a second step below T_N, the bilinear exchange coupling is introduced and using the periodic molecular field model [9, 24] the free energy associated with the three different models of structure was calculated for each set (W, x) previously under test in the paramagnetic range: (i) the fourfold easy axis (the single q model in table 1), (ii) the twofold easy axis (the double q structure in table 2), (iii) the threefold easy axis (the triple q structure in table 3). The most stable magnetic structure is associated with the lowest free energy and consequently with the highest magnetic moment. In these calculations the values for the Fourier transform of the bilinear exchange interactions $J(\mathbf{0})$ and $J(\vec{k})$ ($\vec{k}$ belonging to the $\langle 1/2, 1/2, 0\rangle$ star) are introduced, but for a given (W, x) couple there is no adjustable parameter. Indeed $J(\vec{k})$ is given by

$$J(\vec{k}) = 1/\chi_{CEF}(T_N)$$

where χ_{CEF} is the calculated first order magnetic susceptibility for the given (W, x) couple. The value of $J(\mathbf{0})$ is then deduced from the experimental curve of $1/\chi^{(1)}$ using the relation

$$1/\chi^{(1)}(T_N) = 1/\chi_{CEF}(T_N) - J(\mathbf{0})/(g_J\mu_B)^2.$$

Results show that the single q (fourfold easy axis) structure remains stable in the whole antiferromagnetic phase for $-1 \leqslant x \leqslant -0.2$. In contrast, for x larger than -0.2, calculations predict a spontaneous phase transition from the double q (twofold easy axis) structure at low temperatures towards the triple q one (threefold easy axis) at high temperatures. The value of the temperature of the transition between the double and triple q structures, T_*, was adjusted as a function of x. The best agreement between the calculated transition temperature, $T_{*cal} = 16.6$ K, and the experimental value, $T_* = 16.5$ K, is obtained for $x = -0.145$ and leads to $W = 0.142$ K. The corresponding values of $J(\mathbf{0})$ and $J(\vec{k})$ are respectively -1.3 T μ_B^{-1} ($\approx$27 K) and 0.854 T μ_B^{-1} ($\approx$18 K). This set of CEF parameters corresponds to the following energy level scheme: Γ_7 (0 K), $\Gamma_8^{(1)}$ (16.76 K, 1.44 meV), Γ_6 (26.44 K, 2.27 meV), $\Gamma_8^{(2)}$ (49.95 K, 4.30 meV) and $\Gamma_8^{(2)}$ (69.46 K, 5.98 meV). Coming back to the neutron spectroscopy data such a scheme is apparently consistent with experimental spectra. For $x = -0.145$, the transition probability matrix elements connecting the Γ_7 ground state and the highest excited levels $\Gamma_8^{(2)}$ and $\Gamma_8^{(3)}$ are nearly zero [23]; this may explain the fact that only one transition from the ground state could be observed. According to [23], the features observed in the up-scattering processes, at 20 K around -0.85 and -2.7 meV, can be ascribed to transitions from the first excited level $\Gamma_8^{(1)}$ to the Γ_6 and $\Gamma_8^{(2)}$ levels respectively, and the one around -3.6 meV at 50 K to that from the second excited level Γ_6 to the $\Gamma_8^{(3)}$.

Using the whole set of CEF and bilinear exchange parameters thus determined the magnetic specific heat has been calculated. The results are compared in figure 11 with the experimental data deduced from figure 1 in [15]. Some discrepancies between calculations and experimental

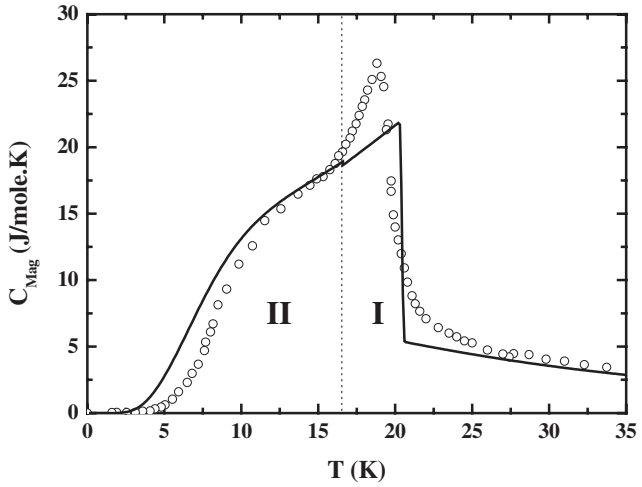

Figure 11. The full curve represents the magnetic specific heat calculated within the periodic molecular field model [9]. The calculations have been performed assuming stabilization of structure b (figure 9) in phase II and structure c (figure 9) in phase I, with the following set of fixed parameters: $W = 0.142$ K, $x = -0.145$, $J(\mathbf{0}) = -1.3$ T μ_B^{-1} and $J(\vec{k}) = 0.854$ T μ_B^{-1}. Calculations are compared with the experimental magnetic specific heat (open dots) deduced from figure 1 in [15].

data are observed: the calculated specific heat is larger than the experimental one below 12 K but becomes smaller above T_*. Nevertheless the main features are reasonably reproduced—for instance the hump below 15 K, the transition temperatures and the contribution in the paramagnetic phase. A latent heat of 0.2 J mol^{-1} is calculated at the transition between the phases I and II. This small value, compared with the variation of 230.4 J mol^{-1} of the internal energy between 0 K and T_N, may account for the fact that experimentally the latent heat could not be observed for polycrystalline samples [15]. In zero field the values of the magnetic moment calculated at 3 and 5.8 K are 8.74 and 8.64 μ_B. They compare well with those deduced from neutron data, respectively 8.83 μ_B at 3 K (powder data [16]) and 8.36 μ_B at 5.8 K (table 2). In phase I the agreement is less good: at 13.8 K the calculated value for the moment is 5.41 μ_B, whereas the refinement for the data collected at 13.8 K gives a value of 6.37 μ_B.

The properties under an applied field are less properly described. For instance calculations clearly confirm a spontaneous transition from the double q structure (phase II) to the four q one (phase III) when increasing the field; however the critical field at low temperatures is calculated at 3.25 T, whereas experimentally the transition is observed at 4.3 T. Also in phase II under low field (0.25 T) the calculated magnetization is about 20% larger than the experimental one at low temperatures.

It turns out that considering only CEF and bilinear exchange couplings one can nicely account for, at least, the spontaneous phase transitions in $DyIn_3$. Though the stabilization of two spontaneous multiple q structures strongly supports the existence of quadrupolar couplings it is pointless, in the absence of an independent experimental confirmation of the CEF scheme, to attempt a quantitative determination of their magnitude. However the existence of a triple q structure with a threefold easy axis attests to the antiferroquadrupolar character of the interactions in the ε symmetry (Γ_5). This leads to the following relation for the Fourier transforms of the quadrupolar coefficients: $K^{\varepsilon}(0) < K^{\varepsilon}(1/2, 1/2, 0)$ [3]. The existence of a double q with a twofold easy axis reveals in contrast ferroquadrupolar coupling in the γ symmetry (Γ_3): $K^{\gamma}(1/2, 1/2, 0) < K^{\gamma}(0)$.

In the paramagnetic range the first and third order magnetic susceptibilities were calculated within the CEF susceptibility formalism [2] using the set of parameters previously determined: $W = 0.142$ K, $x = -0.145$. Good fits between calculated and experimental data are obtained with $\theta_p = -32$ K (see figures 6 and 7). This value of θ_p is in good agreement with that of $J(\mathbf{0})$ determined at T_N. In the calculations of the third order magnetic susceptibility (figure 7) G_1 represents the total quadrupolar parameter as defined in [2]:

$$G_1 = \frac{(B^\mu)^2}{C_0^\mu} + K^\mu, \qquad \mu = \varepsilon, \gamma$$

where B^μ represents the magneto-elastic coefficient, C_0^μ the background symmetrized elastic constant and K^μ the two ion quadrupolar coefficient. Along the threefold and fourfold symmetry axes G_1 retains very weak values, ≈ -1.5 to -5 mK; the main effect comes from θ_p. As expected, the third order susceptibility variation along the twofold axis is intermediate between the threefold and fourfold variations. As no measurements of the elastic constant or parastriction have been performed on $DyIn_3$, the values of the coefficients $K^\mu(0)$ remain undetermined. However comparing the values of G_1 and $K^\mu(0)$ deduced for $TbIn_3$ [21] leads us to suppose that the coefficients $K^\mu(0)$ remain weak in $DyIn_3$. In the paramagnetic phase of $DyIn_3$ also the magnetic properties are clearly dominated by the CEF interactions and bilinear exchange couplings.

6. Conclusions

Bulk magnetization studies on $DyIn_3$ have confirmed the metamagnetic behaviour of the magnetization in the ordered phase and allowed us to determine the magnetic phase diagrams. Systematic measurements along the twofold axis have revealed a complex phase diagram with at least five phases. Only three of these phases could be probed by the neutron diffraction technique. The analysis of all the neutron diffraction data allowed us to sketch a coherent interpretation of the low field phase diagram: stabilization of a three q structure below T_N and transition towards a double q structure at T_*. Neutron spectroscopy results have definitively ruled out the set of CEF parameters previously reported in the literature [15]. Within the periodic molecular field model we determine here a new set of CEF parameters: $W = 0.142$ K, $x = -0.145$ or $A_4\langle r^4\rangle = 5.8$ K, $A_6\langle r^6\rangle = 8.5$ K, consistent with the neutron spectroscopy data, which account for the spontaneous phase transition at $T_* = 16.5$ K in the antiferromagnetic range. It turns out that with this set of CEF parameters the behaviour of $DyIn_3$ can be described in the ordered phase without bringing in the quadrupolar interactions. The analysis of the third order magnetic susceptibility in the paramagnetic phase confirms that the total quadrupolar parameters are at least one order of magnitude smaller than those determined in $NdIn_3$ [19] and $TbIn_3$ [21]. Though quadrupolar interactions are necessary to stabilize the multiple q magnetic structures in $DyIn_3$, the CEF and the bilinear coupling, alone, account nicely for the magnetic properties.

References

[1] Gignoux D and Schmitt D 1997 *Handbook of Magnetic Materials* vol 10, ed K H J Buschow (Amsterdam: Elsevier) chapter 2, p 239
[2] Morin P and Schmitt D 1990 *Ferromagnetic Materials* vol 5, ed E R Wohlfarth and K H J Buschow (Amsterdam: North-Holland) chapter 1, p 1
[3] Amara M and Morin P 1995 *Physica* B **205** 379
[4] Kaneko T, Yosida H, Ohashi M and Abe S 1987 *J. Magn. Magn. Mater.* **70** 277
[5] Morin P and Schmitt D 1980 *J. Magn. Magn. Mater.* **21** 243

[6] Morin P, Rouchy J, Schmitt D and du Trémolet de Lacheisserie E 1990 *J. Magn. Magn. Mater.* **90/91** 105
[7] Morin P, Rouchy J, Yonenobu K, Yamagishi A and Date M 1989 *J. Magn. Magn. Mater.* **81** 247
[8] Amara M, Morin P and Burlet P 1995 *Physica* B **210** 157
[9] Amara A and Morin P 1996 *Physica* B **222** 61
[10] Morin P, Giraud M, Burlet P and Czopnik A 1987 *J. Magn. Magn. Mater.* **68** 107
[11] Stalinski B, Czopnik A, Iliev N and Mydlarz T 1979 *J. Physique Coll.* C5 **40** 149
[12] Czopnik A, Mädge H and Stalinski B 1986 *Phys. Status Solidi* a **94** K13
[13] Czopnik A, Mädge H, Pott R and Stalinski B 1988 *Phys. Status Solidi* a **110** 601
[14] Czopnik A, De Boer F R, Veenhuizen P A, Gren B and Stalinski B 1990 *Physica* B **167** 49
[15] Czopnik A, Elenbaas R A and Mattens W C M 1991 *Phys. Status Solidi* a **123** 285
[16] Galéra R M and Morin P 1992 *J. Magn. Magn. Mater.* **116** 159
[17] Amara M, Galéra R M, Morin P, Veres T and Burlet P 1994 *J. Magn. Magn. Mater.* **130** 127
[18] Amara M, Galéra R M, Morin P, Voiron J and Burlet P 1994 *J. Magn. Magn. Mater.* **131** 402
[19] Amara M, Galéra R M, Morin P, Voiron J and Burlet P 1995 *J. Magn. Magn. Mater.* **140–144** 1157
[20] Amara M, Morin P and Rouchy J 1994 *J. Magn. Magn. Mater.* **130** 115
[21] Galéra R M, Amara M, Morin P and Burlet P 1998 *J. Phys.: Condens. Matter* **10** 3883
[22] Lea K R, Leask M J M and Wolf W P 1962 *J. Phys. Chem. Solids* **23** 1381
[23] Birgeneau R J 1972 *J. Phys. Chem. Solids* **33** 59
[24] Blanco J A, Gignoux D and Schmitt D 1991 *Phys. Rev.* B **43** 13145